Available online at www.sciencedirect.com
ScienceDirect
Journal of Computational Physics 217 (2006) 473–484
JOURNAL OF COMPUTATIONAL PHYSICS
www.elsevier.com/locate/jcp

Revisiting the Rossby–Haurwitz wave test case with contour advection

Robert K. Smith, David G. Dritschel *

School of Mathematics and Statistics, Mathematical Institute, University of St. Andrews, North Haugh, St. Andrews, KY16 9SS, UK

Received 22 September 2005; received in revised form 5 January 2006; accepted 6 January 2006
Available online 3 March 2006

Abstract

This paper re-examines a basic test case used for spherical shallow-water numerical models, and underscores the need for accurate, high resolution models of atmospheric and ocean dynamics. The Rossby–Haurwitz test case, first proposed by Williamson et al. [D.L. Williamson, J.B. Drake, J.J. Hack, R. Jakob, P.N. Swarztrauber, A standard test set for numerical approximations to the shallow-water equations on the sphere, J. Comput. Phys. (1992) 221–224], has been examined using a wide variety of shallow-water models in previous papers. Here, two contour-advective semi-Lagrangian (CASL) models are considered, and results are compared with previous test results. We go further by modifying this test case in a simple way to initiate a rapid breakdown of the basic wave state. This breakdown is accompanied by the formation of sharp potential vorticity gradients (fronts), placing far greater demands on the numerics than the original test case does. We also go further by examining other dynamical fields besides the height and potential vorticity, to assess how well the models deal with gravity waves. Such waves are sensitive to the presence or not of sharp potential vorticity gradients, as well as to numerical parameter settings. In particular, large time steps (convenient for semi-Lagrangian schemes) can seriously affect gravity waves but can also have an adverse impact on the primary fields of height and velocity. These problems are exacerbated by a poor resolution of potential vorticity gradients.

Keywords: Contour advection; Shallow-water equations; Spherical geometry; Rossby waves; Potential vorticity

1. Introduction

1.1. The shallow-water model

The shallow-water equations (SWEs) describe the motion of a thin layer of fluid held down by gravity. They have been widely used as a simple model of large-scale atmospheric and oceanic dynamics. They are capable of describing diverse nonlinear fluid phenomena, including vortices and gravity waves, over a broad range of spatial and temporal scales. Yet, this flexibility means that a comprehensive understanding of their solution properties is difficult to achieve.

* Corresponding author. Tel.: +44 1334 463721; fax: +44 1334 463748.
E-mail address: dgd@mcs.st-and.ac.uk (D.G. Dritschel).

0021-9991/$ - see front matter © 2006 Elsevier Inc. All rights reserved.
doi:10.1016/j.jcp.2006.01.011

Inevitably, studying complex flows such as the atmosphere and the oceans requires accurate numerical simulation. The SWEs are a convenient, relatively simple testbed for numerical methods. Many numerical issues need to be considered, particularly when designing global methods in spherical geometry. It is fair to say, however, that most existing test cases only mildly challenge numerical methods, and certainly they hardly reflect the true complexity of observed fluid flows.

Here, we revisit one of these test cases, proposed by Williamson et al. [21], but also consider a simple variation of it which permits realistic flow complexity in a short integration time. This test case involves a Rossby–Haurwitz wave, a steadily propagating global solution only in the barotropic limit (vanishing Froude number). The original test exhibits nearly steady motion, but this breaks down into more turbulent behaviour at late times as recently discovered by Thuburn and Li [20]. The variation considered here includes an initial broad-scale perturbation which promotes a rapid break down. It proves significantly more challenging to achieve numerical convergence for this more realistic flow.

1.2. Overview of the basic equations

The equations expressing momentum balance and mass continuity for an inviscid, adiabatic fluid are:

$$\frac{\mathrm{D}\mathbf{u}}{\mathrm{D}t} + 2\underline{\Omega} \times \mathbf{u} = -\nabla \Phi \tag{1}$$

$$\frac{\partial \Phi}{\partial t} + \nabla \cdot (\Phi \mathbf{u}) = 0 \tag{2}$$

(e.g. see [8,15] and references therein) where $\mathbf{u}$ is the layer mean horizontal velocity, $\Phi = gh$ is the geopotential, proportional to the hydrostatic pressure, h is the local fluid height and $\underline{\Omega}$ is the Earth's rotation vector. In Eq. (1), only components parallel to the Earth's surface are retained. Taking (x, y, z) as local coordinates pointing eastwards, northwards and upwards, respectively, the velocity $\mathbf{u} = (u, v)$ consists of just two components, u and v, directed eastward and northward, respectively. On a sphere of radius a, $\mathrm{d}x = r\,\mathrm{d}\lambda$ and $\mathrm{d}y = a\,\mathrm{d}\phi$, where λ and ϕ denote longitude and latitude, and $r \equiv a\cos\phi$ is the horizontal radius. Instead of using the two velocity components u and v, many numerical algorithms use vorticity ζ and divergence δ, defined by:

$$\zeta = \frac{1}{r}\frac{\partial v}{\partial \lambda} - \frac{1}{r}\frac{\partial}{\partial \phi}(ru) \tag{3}$$

$$\delta = \frac{1}{r}\frac{\partial u}{\partial \lambda} + \frac{1}{r}\frac{\partial}{\partial \phi}(rv) \tag{4}$$

as the prognostic variables (most convenient for spectral models). The height is also separated into a constant mean value H and a deviation h' to define the mean short-scale gravity wave speed $c = \sqrt{gH}$ and a dimensionless height anomaly $\tilde{h} = h'/H$.

The equations, in terms of ζ, δ and $\tilde{h}$ are:

$$\frac{\partial \zeta}{\partial t} + f\delta = -\nabla \cdot (\mathbf{u}\zeta) \tag{5}$$

$$\frac{\partial \delta}{\partial t} + c^2 \nabla^2 \tilde{h} - f\zeta = -\nabla \cdot (\mathbf{u} \times \nabla \mathbf{u}) \tag{6}$$

$$\frac{\partial \tilde{h}}{\partial t} + \delta = -\nabla \cdot (\mathbf{u}\tilde{h}) \tag{7}$$

where $f = 2\Omega\sin\phi$ is the Coriolis frequency (cf. [12]). The velocity components are obtained from ζ and δ by solving Poisson equations for the stream function ψ and divergence potential χ:

$$\nabla^2 \psi = \zeta \tag{8}$$

$$\nabla^2 \chi = \delta \tag{9}$$

with

$$\mathbf{u} = \mathbf{k} \times \nabla\psi + \nabla\chi \tag{10}$$

However, either variable choice (u, v, h) or $\{\zeta, \delta, \tilde{h}\}$ hides potential vorticity conservation. Eqs. (5) and (7) together imply

$$\frac{Dq}{Dt} = \frac{\partial q}{\partial t} + \mathbf{u} \cdot \nabla q = 0 \tag{11}$$

where

$$q = \frac{\zeta + f}{1 + \tilde{h}} \tag{12}$$

is the potential vorticity (hereafter PV). PV is a unique variable, not only because of its material conservation, but also because of the role it plays in 'balance' or 'PV inversion' ([4,7,10,12,14] and references).

1.3. The numerical method

A previous comparative study ([3], hereafter 'DPM99') demonstrated that explicit PV conservation can greatly improve the accuracy of shallow-water simulations in the *f*-plane context. Here, we extend this approach to spherical geometry. The model used here, called CA_0, replaces Eq. (5) with Eq. (11), thus making the prognostic variables $\{q, \delta, \tilde{h}\}$. The PV is represented in a fully Lagrangian way as material contours between which the PV is uniform and across which it jumps by a specified value Δq (see [2] for details). This is the basis of "Contour Advection". Other variables are held on a grid, and evolved in a conventional way. A common grid for spherical spectral models takes the number of points in latitude to be half the number of points in longitude, i.e., $n_\phi = n_\lambda/2$. Here though we use a semi-spectral approach with second-order finite differencing in latitude and Fourier series in longitude. Extra resolution is used in latitude to compensate for the higher errors in finite differencing compared to Fourier (Legendre) series. By experimentation, using $n_\phi = n_\lambda$ was found to be optimal, in terms of representing the velocity field, when balancing accuracy and efficiency for flows having sharp vorticity gradients. Indeed, for a vorticity discontinuity, one may show that the formal accuracy of the spectral approach is no greater than that for second-order finite differences [19].

Time stepping of δ and $\tilde{h}$ makes use of the standard semi-implicit leap-frog procedure [17], with a Robert–Asselin filter [1,18] to ensure stability. After extensive testing, we found that the filter coefficient A can be chosen as small as $c\Delta t/a$, where Δt is the time step and a is the Earth's mean radius [19]. For large time steps, A is limited to 0.2.

While not explicit in the basic equations, some kind of numerical diffusion is often added to reduce aliasing errors and filter poorly resolved short-scale (and typically high-frequency) motions. The explicit use of PV in CA_0 permits much weaker diffusion for stability (DPM99) – much of the difficulty faced by conventional models stems from their inability to resolve sharp gradients of PV (fronts) and small-scale filamentary structures, common features in the atmosphere and oceans. Even in contour advection, it is impossible to keep up with this scale cascade entirely, and thin filaments are removed by 'surgery' (cf. [2] and references), here at a tenth of the latitude spacing of grid points. This however results in much better *material* conservation of PV than is possible in conventional methods (DPM99). For the fields δ and $\tilde{h}$, a 'Broutman' spectral filter is applied to their nonlinear tendencies (cf. [4]). This filter is applied in longitude only, and essentially removes all azimuthal variations shorter than two grid lengths at the equator (where the upper third wavenumbers $m > n_\lambda/3$ are strongly damped). The specific form used is $F(m) = \exp[-\alpha(\xi/r)^{10}]$, for $m \geqslant 2$, where $\xi = (m - 2)/(M - 2)$, $M = n_\lambda/2$ and α is chosen so that $F(M) = 10^{-14}$. Wavenumbers $m = 0$ and 1 are not damped. Approaching the poles, $r \to 0$, an increasing proportion of wavenumbers are filtered. This is consistent with the decreasing spacing of longitudes. If one omits the $r = \cos\phi$ factor, the filter is not adequate to ensure numerical stability in polar regions.

The above, purely longitudinal filter, is often sufficient for numerical stability. But occasionally numerical noise develops in latitude, and some damping appears to be necessary. Here, this is done by adding latitudinal diffusion to the δ and $\tilde{h}$ tendencies (using the discrete Laplacian operator). Only a very small damping rate of $D = 0.01$ per day was necessary at the equivalent maximum wavenumber in latitude. The results are insensitive to this coefficient, as shown below.

2. The Rossby–Haurwitz wave test

Rossby–Haurwitz waves are steadily propagating solutions of the fully nonlinear non-divergent barotropic vorticity equation on the sphere [9]. This case is useful for testing numerical models as it can be described exactly by analytic formulae and, although the SWEs do not have analytic solutions, a Rossby–Haurwitz initial condition is expected to evolve nearly steadily. This motivated Williamson et al. [21] to propose Rossby–Haurwitz waves as one of seven standard test cases.

In the following, as in all previous tests, a zonal wavenumber of 4 is used. It was believed that a zonal wavenumber greater than 5 was unstable, but as recently shown in Thuburn and Li [20], this case is actually also weakly unstable and will eventually break down once perturbed. In fact, even truncation errors cause instability.

2.1. The initial flow

A complete description of the test case is given by Williamson et al. [21], so only a few key aspects are noted here. The initial velocity is non-divergent ($\delta = 0$) with the streamfunction given by

$$\psi = -a^2\omega \sin\phi + a^2 K \cos^4\phi \sin\phi \sin 4\lambda \qquad (13)$$

where $a = 6.37122 \times 10^6$ m and $\omega = K = 7.848 \times 10^{-6}$ s^{-1}.

The initial height field h is chosen to be "in balance with" the velocity field, by requiring the initial divergence tendency to be zero (the analytical form of h is given in [21]). The minimum fluid height occurs at the poles, where $h = 8000$ m, and the mean fluid height is $H = 9523$ m. We use a height contour interval of 120 m, and a PV contour interval of 9.3385×10^{-6} s^{-1} to compare directly with Thuburn and Li [20]. The initial height and PV fields are shown in Fig. 1.

Using a variety of numerical parameters, the CA_0 model was run for 40 days. The benchmark case employed a resolution of 128×128, a time step of $\Delta t = 0.0025$ of a day (a little less than half the CFL time step $\Delta t_{CFL} = \Delta\phi/c = 0.0059387$, where $c = 305.59$ m s^{-1}), and a latitudinal damping coefficient of $D = 0.01$. The results at early times (see below) closely reproduce those found by Thuburn and Li [20] using independent models.

2.2. Why revisit this test case?

While this test case has been carried out in many previous studies, attention has been largely focused on the early time evolution of the height field, which exhibits little variation – see Fig. 2. Thuburn and Li [20] illustrate the PV as well, which is also a simple field at early times (they show day 8). They also take the test case further in time and find that the stability of the Rossby–Haurwitz wave is sensitive to numerical error. In particular, the flow breaks down between 30 and 40 days, depending on numerical parameters and the model employed.

Qualitatively similar behaviour is found when using the CA_0 model. The flow becomes noticeably unstable around day 30. By day 35, the PV and divergence fields have become turbulent, as exhibited in Fig. 3. PV gradients sharpen into virtual discontinuities, fronts, which dominate the subsequent evolution. The divergence

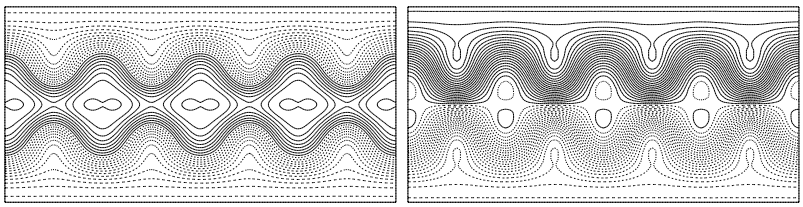

Fig. 1. Initial Rossby–Haurwitz height anomaly (left) and PV (right) fields, plotted as a function of longitude $-\pi < \lambda < \pi$ and latitude $-\pi/2 < \phi < \pi/2$. Positive contour levels are solid, while negative ones are dashed. Contour levels displayed are $\pm\Delta/2$, $\pm 3\Delta/2$, etc., where Δ is the contour interval.

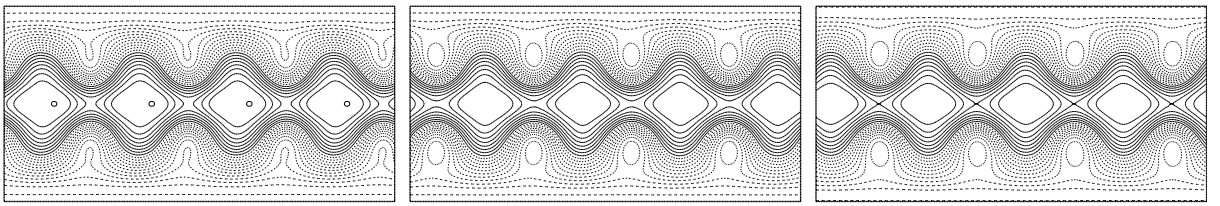

Fig. 2. Height anomaly field at days 3, 6 and 9 (left to right): cf. Thuburn and Li [20].

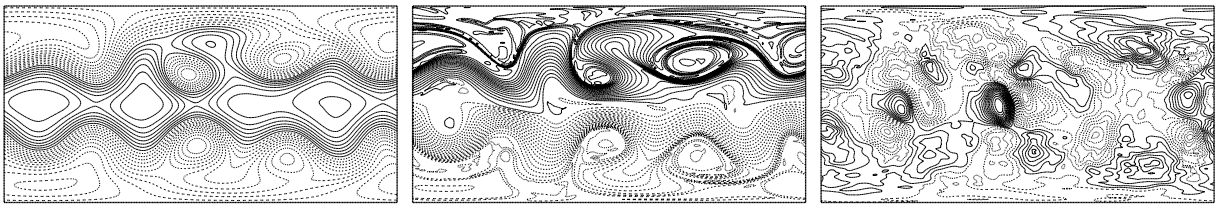

Fig. 3. Height anomaly, PV and divergence fields (left to right) at day 35. The divergence contour interval is 0.001 days^{-1} in this and subsequent figures.

field becomes highly structured, only in part from gravity waves (see below). This complex late time behaviour was not anticipated in the design of this test case, but it is in fact more characteristic of realistic atmospheric and oceanic flows than is the simple early time behaviour.

This turbulent flow puts severe demands on the numerics, at least if one tries to maintain accuracy. Numerical parameters, particularly the time step and the diffusion coefficient, need to be carefully chosen to represent the flow – both the vortical part and the gravity wave part – as accurately as possible while keeping numerical stability. This is a difficult balancing act, as both accuracy and stability are flow dependent.

The key point is that the test case must be sufficiently demanding for numerical methods intended for the core of more realistic atmospheric and oceanic models (as advocated by DPM99). This means the flow should ideally exhibit a degree of complexity comparable to that found in naturally-occurring flows, which contain sharp PV gradients and abundant fine-scale structure. The test case must also be reproducible, i.e., (1) insensitive to numerical noise and (2) convergent with increasing spatial and temporal resolution over a period of time during which the flow changes non-trivially. These are somewhat conflicting requirements, as a more complex flow is generally less predictable than a simple flow. As a result, few demanding and reproducible test cases exist.[1]

3. Modification of the Rossby wave test

There is a simple way to modify the present test case to ensure that the test case is both demanding and reproducible over a moderately long period of time. This is done by adding an (unbalanced) global-scale, small-amplitude height anomaly $\tilde{h}$ at $t = 0$. (In practise, this gives rise to very weak gravity waves which are barely detectable in the subsequent flow evolution.) The disturbance takes the form $(xx_0 + yy_0 + zz_0)/40a^2$, where (x,y,z) are the Cartesian coordinates of a point on the sphere, and (x_0,y_0,z_0) is a specific point located at latitude $\phi = 40°$ and longitude $\lambda = 50°$. This is simply added to the balanced field described in Section 2.1.

Using the benchmark settings (128×128 resolution, $\Delta t \approx 0.43521 \Delta t_{\mathrm{CFL}}$, and a damping coefficient $D = 0.01$), the flow evolution is shown in Fig. 4. Within just a few days the flow breaks down into a complex assortment of fronts and vortices, most evident in the PV field. (The maximum Froude number $|\mathbf{u}|/c_0 = \max |\tilde{h}|^{1/2}$ reaches 0.435 (the time mean is 0.35) and the minimum and maximum 'Rossby numbers' $\zeta/2\Omega$ reach ≈ -0.80 and 0.87.) The height field distorts significantly but remains broad-scale. In particular, there is no visible trace of gravity waves in this field.

[1] Appropriate test cases – with topographic forcing – have been developed by Juckes and McIntyre [11] and Williamson et al. [21].

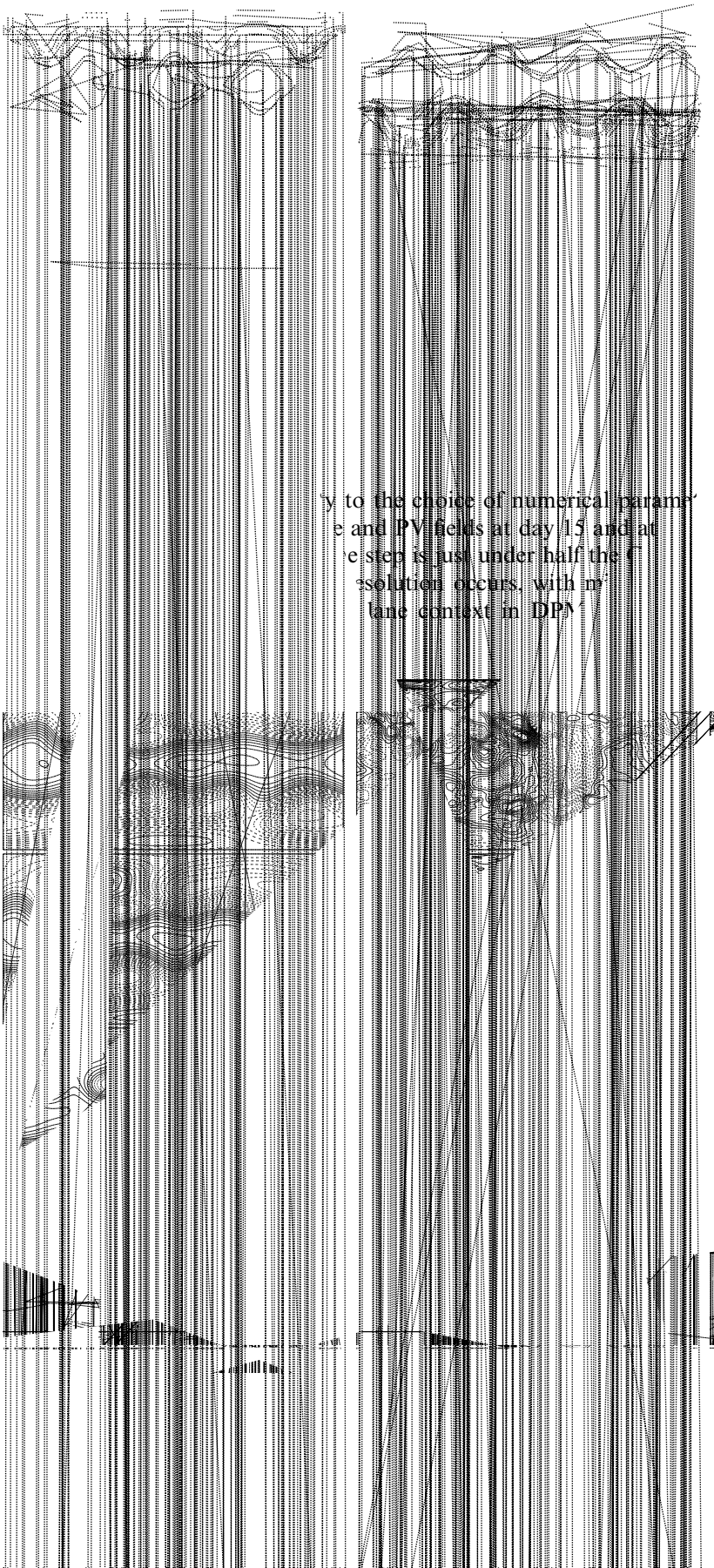

y to the choice of numerical parame . he effe
e and PV fields at day 15 and at ions $64 \times$
e step is just under half the (: (s it va
esolution occurs, with m ces ve
lane context in DPV ave

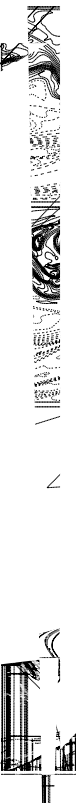

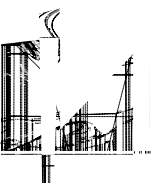

between the highest resolution case and the others are 1.71%, 7.41% and 26.0%, for 256×256, 128×128 and 64×64, respectively (these are percentages of the r.m.s. height anomaly in the highest resolution case). The PV differences are 3.00%, 7.87% and 19.1%. The differences diminish sharply with resolution, most strongly for the smoother height field, as expected. The PV differences are created by advection errors, arising mainly from errors in the velocity field. Numerical convergence is less marked for the divergence field, which exhibits errors of 16.0%, 33.6% and 60.4% (i.e., only inversely proportional to spatial resolution). The instantaneous errors grow in time as the solutions diverge, but the dependence on resolution is similar – see Fig. 6.

As elaborated in the following section, a significant part of this error arises from the poor numerical representation of the underlying PV-controlled balanced motions when using $\tilde{h}$ and δ as prognostic variables (see [13,14]). This leads to excessive noise, particularly near the poles (seen here in δ at the two highest resolutions), which can sometimes cause the model to blow up, even with larger latitudinal damping. This noise does not develop in the more advanced model, CA_1, described in the following section.

The effect of time step is shown in Fig. 7, for the height field at day 15 and for time steps $\Delta t = 0.00125$, 0.0025, 0.005, 0.01, 0.02 and 0.04 (corresponding to 0.210, 0.43521, 0.842, 1.684, 3.368 and $6.735\Delta t_{\mathrm{CFL}}$) (note: Thuburn and Li [20] used Δt □ $7\Delta t_{\mathrm{CFL}}$). The time-averaged r.m.s. height differences between the finest time step case and the others (in order of increasing Δt) are 0.534%, 1.11%, 2.25%, 4.81% and 7.59%. (The corresponding PV differences are 0.436%, 0.744%, 1.33%, 1.48% and 3.94%.) Using larger time steps is not nearly as detrimental as using coarser spatial resolution, but errors are clearly noticeable for time steps much is excess of t_{CFL}. Moreover, divergence differences are much larger, coming in at 40.2%, 49.4%, 56.0%, 68.4% and 78.6% in order of increasing time step. These errors stem in part from the semi-implicit scheme, which couples the equations for height and divergence, fields which are often very different in character. The height field tends to be dominantly balanced and slowly evolving (like the

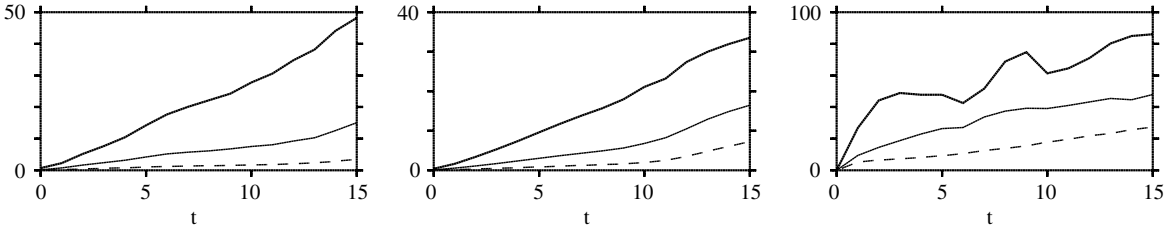

Fig. 6. Instantaneous percentage r.m.s. error in height anomaly (left), PV (middle) and divergence (right) versus time. The errors are computed relative to the average r.m.s. field amplitudes in the highest resolution case.

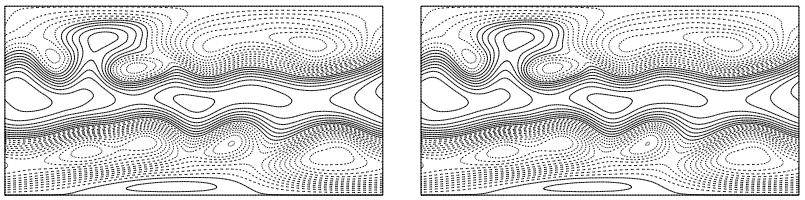

Fig. 8. Effects of varying damping on the perturbed height anomaly field at day 15. Damping coefficients 0.1 and 0.01 are compared (left and right).

PV), while the divergence tends to contain significantly more high frequency motions, i.e., gravity waves. Simply slowing down the waves in the semi-implicit scheme does not eliminate them – indeed they may be more easily excited by the vortical motions. This coupling can and arguably should be avoided, as the results of the following section demonstrate.

Finally, the damping coefficient has no perceptible impact on the solution accuracy, for $0.01 \leqslant D \leqslant 0.1$ – see Fig. 8. Time-averaged r.m.s. differences in $\tilde{h}$, δ and PV are just 0.314%, 4.82% and 0.435%. Values of D smaller than 0.01 however lead to numerical instability in some cases. Doubling the Robert–Asselin filter coefficient results in differences of 0.258%, 8.15% and 0.286% for the three fields. As expected, the time filter principally affects the divergence field due to the presence of gravity waves.

4. An improved numerical method

4.1. Introduction to CA_1

Previous work [4,13] identified a new approach to significantly improving solution accuracy at little extra computational cost. The CA_0 model differs from conventional models principally in the way that it handles PV conservation. Otherwise, it uses standard variables, at least for spectral models. But there is another important aspect of PV which is not treated explicitly, namely the way in which PV controls much of the fluid motion, through underlying 'balance relations' [10,12]. For example, at small Rossby and Froude numbers, geostrophic balance may be expected to hold everywhere except near the equator. This balance implies that the height field is instantaneously related to the PV field (in general via an elliptic operator). Now suppose one tried to run a shallow-water model under these conditions, with the height field as one of the prognostic variables. Balance implies there is a direct link between height and PV at any time, but the numerics does not see this and instead integrates the height field as an independent variable. Of course it should, one might believe, in order to also capture gravity waves, motions not part of the balance. But the problem is that numerical discretisation errors, both in space and in time, make it difficult to maintain the underlying balance, and the errors show up erroneously as gravity waves.

A way around this problem is to use a set of prognostic variables which better distinguishes balanced motions and gravity waves, ideally PV and a pair of 'wave' variables [4,13,14]. The idea is to represent the *departure* from balance by these 'wave' variables. Then, to recover the original variables $\tilde{h}$, u and v, one solves a series of elliptic problems, like in 'PV inversion' [12] but involving the complete set of new variables (see below). The crucial point is that these elliptic problems *reduce* to balance relations when the 'wave' variables are ignored. This feature leads to a significant reduction in erroneous gravity waves, and it improves the prediction of the dominant balanced motions.

In reality, there is no pair of variables that represent pure gravity waves for nonlinear flows, and efficiency considerations force a compromise. Here, we use a pair of variables that proved optimal in the f-plane context [13], taking into account robustness, accuracy, and efficiency. One of the variables is the velocity divergence $\delta = \nabla \cdot \mathbf{u}$, already used in CA_0. The other is the acceleration divergence

$$\gamma = \nabla \cdot \frac{\mathrm{D}\mathbf{u}}{\mathrm{D}t} = f\zeta - \beta u - c^2 \nabla^2 \tilde{h} \qquad (14)$$

where $\beta = \mathrm{d}f/\mathrm{d}\phi = 2\Omega\cos\phi$ [5]. In the f-plane context, γ/f is the 'ageostrophic vorticity'.

The prognostic equations for δ and γ are obtained using Eqs. (5) and (7), and may be written as:

$$\frac{\partial \delta}{\partial t} = \gamma + |\mathbf{u}|^2 - 2\left[\frac{\partial u}{\partial \phi}\left(\frac{\partial u}{\partial \phi} + \zeta\right) + \frac{\partial v}{\partial \phi}\left(\frac{\partial v}{\partial \phi} + \delta\right)\right] - \nabla\cdot(\delta\mathbf{u}) \tag{15}$$

$$\frac{\partial \gamma}{\partial t} = c^2\nabla^2\delta + c^2\nabla\cdot(\tilde{h}\mathbf{u}) + 2\Omega\frac{\partial B}{\partial \lambda} - \nabla\cdot(Z\mathbf{u}) \tag{16}$$

where $B = c^2\tilde{h} + \frac{1}{2}|\mathbf{u}|^2$ is the Bernoulli pressure and $Z \equiv f(\zeta + f)$. This model is referred to as CA_1.

Eq. (15) is written in a non-standard way to avoid any spatial derivatives on ζ (which are infinite for a PV jump) and second derivatives on $\mathbf{u}$ (which are also infinite for a PV jump). While these derivatives cancel mathematically, they do not numerically due to discretisation errors. This strategy was adopted also in the f-plane context [3]. Finally, to avoid centred-differencing errors in latitude, the latitude derivatives in Eq. (15) are replaced by ζ, δ, and longitude derivatives using Eqs. (3) and (4). (Longitude derivatives are computed spectrally.)

To evaluate the field tendencies and to advect the PV contours, the primitive variables $(\tilde{h}, u, v)$ must be recovered from the new ones (q, δ, γ). This "inversion" is done as follows. First, the divergence potential χ is recovered directly from δ using Eq. (9). This then gives the divergent part of the velocity field from Eq. (10). The non-divergent part involving ψ however requires ζ, which depends on q and $\tilde{h}$. So, we need $\tilde{h}$ to proceed. An equation for $\tilde{h}$ is available in the definition of γ, which however depends on u and hence ψ. So, the equations for $\tilde{h}$ and ψ are coupled. But, they are both linear, given (q, δ, γ). In practise, the equations are solved iteratively, rewriting Eq. (14) as

$$c^2\nabla^2\tilde{h} - f^2\tilde{h} = f(\zeta - f\tilde{h}) - \beta u - \gamma \tag{17}$$

with terms on the right-hand-side evaluated using previous iterates. Numerically, these equations converge exponentially fast, so that only a few iterations are required to achieve convergence (here when the maximum pointwise difference between successive $\tilde{h}$ iterates is less that 10^{-8}).

4.2. CA_1 results

First of all, no latitudinal damping was found to be necessary for CA_1. Divergence fields are noticeably smoother, not because of diffusion, but because the underlying balance is better respected.

At early time periods, the CA_0 and CA_1 results differ negligibly for the original Rossby–Haurwitz wave test. But this only tests the correctness of the numerical model. To test accuracy, we need to look at how the models deal with a complex flow having a wide range of spatial and temporal scales. We focus on the perturbed Rossby–Haurwitz case, which destabilises quickly and reproducibly. At the benchmark resolution, 128×128 and $\Delta t = 0.5\Delta t_{\mathrm{CFL}}$, the height and PV fields differ little between the models, see Figs. 9 and 10 which compare the main fields given by CA_0 and CA_1, but the divergence field is significantly smoother in CA_1. Movies of the dynamical evolution show that the pattern of δ moves with the PV, indicating that even δ is dominantly balanced in this flow. Time-averaged r.m.s. differences between the fields in the two models are 1.77%, 8.62% and 2.46%, for $\tilde{h}$, δ and PV, respectively (these drop to 0.440%, 3.69% and 0.948% at 256×256 resolution). Note that the divergence difference is most significant. Convergence is faster in CA_1, as seen for instance when comparing time steps of $\Delta t = 0.00125$ and $\Delta t = 0.0025$, for which $\tilde{h}$, δ and PV differences are 0.413%, 21.7% and 0.349%, compared to 0.534%, 40.2% and 0.436% in CA_0. Also, when comparing 512×512 and 256×256 resolutions, $\tilde{h}$, δ and PV differences are 1.52%, 15.4% and 2.69% in CA_1, while they are 1.71%, 16.0% and 3.00% in CA_0. This indicates that the time step is the most important factor for the accuracy of the divergence field. This is likely due to the presence of significant gravity wave activity in δ (and in γ, see below), whose higher frequency components are better resolved with a shorter time step. Such fast motions are virtually absent in $\tilde{h}$ and q.

The field of acceleration divergence γ, never previously illustrated, is shown in Fig. 11 at times corresponding to Figs. 9 and 10. This field is more highly structured than δ, with many more small-scale features. Largest values occur within strong cyclonic vortices, which tend to be more ageostrophic than anti-cyclonic vortices in shallow-water flows [16]. Again however the pattern of γ largely follows PV (not shown), indicating that γ like δ is dominantly balanced. Ideally, we would like to use a better choice of 'wave' variables, e.g. the first time

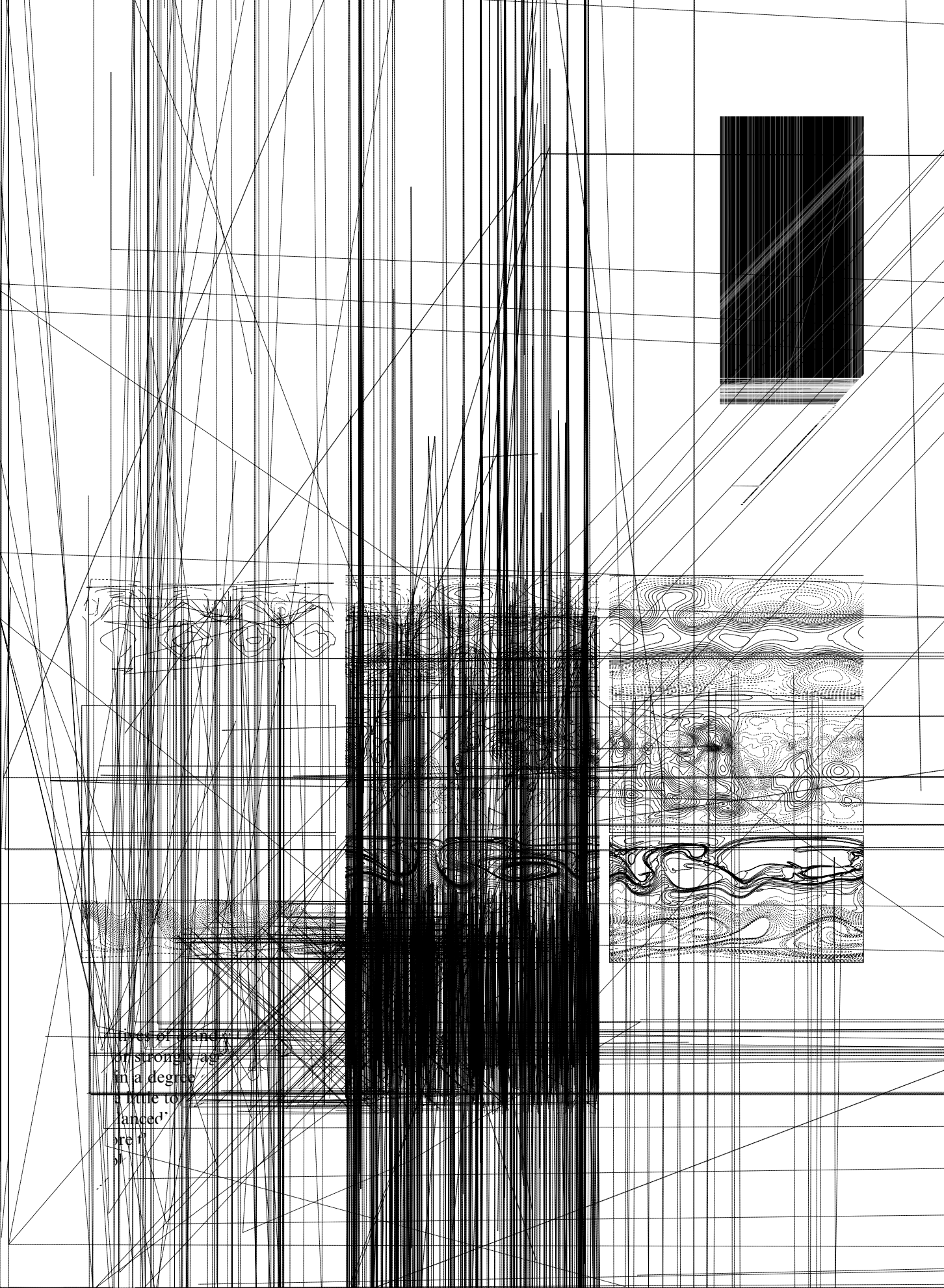

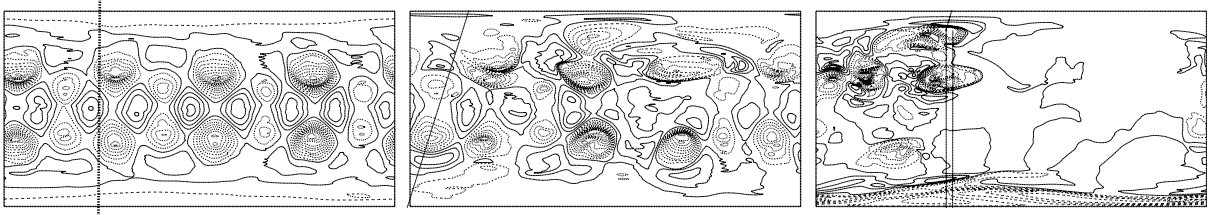

5. Conclusion

We have revisited one of the standard test cases proposed for the shallow-water equations in spherical geometry using an explicitly PV-conserving contour-advection model. Our results closely reproduce previous results obtained with a variety of different models at early times. At late times, Thuburn and Li [20] demonstrated that this simple test breaks down into a complex turbulent flow. This suggested a small modification of the original test to exploit the physical instability and obtain a rapid and reproducible turbulent breakdown of the original flow. This, we argue, is a better test for numerical methods being considered for implementation in more realistic global atmospheric and oceanic models. The flow develops a wide range of spatial and temporal scales, and properly challenges numerical models. This is important.

The new contour advection model introduced here copes well with this complexity by explicitly conserving PV and preserving dynamically active sharp gradients (fronts). This is a major advantage of contour advection, and one which is not lessened when non-conservative diabatic effects are taken into account [6]. We also found that it is important to preserve the underlying balance, the implicit control exerted by PV, in these flows. To this end, we extended an idea, first implemented in the *f*-plane context, of using a new set of prognostic variables which distinguishes balanced vortical motions and unbalanced gravity waves, at least to leading order [13]. At little extra computational expense, this significantly improves the accuracy of the balanced part of the flow, and in turn, the unbalanced part as well. This simple idea may be worthwhile extending to more realistic contexts.

References

[1] R. Asselin, Frequency filter for time integrations, Mon. Weather Rev. 100 (1972) 487–490.

[2] D.G. Dritschel, M.H.P. Ambaum, A contour-advective semi-Lagrangian algorithm for the simulation of fine-scale conservative fields, Quart. J. Roy. Meteorol. Soc. 123 (1997) 1097–1130.

[3] D.G. Dritschel, L.M. Polvani, A.R. Mohebalhojeh, The contour-advective semi-Lagrangian algorithm for the shallow water equations, Mon. Weather Rev. 127 (1999) 1551–1565.

[4] D.G. Dritschel, Á. Viúdez, A balanced approach to modelling rotating stably stratified geophysical flows, J. Fluid Mech. 488 (2003) 123–150.

[5] D.G. Dritschel, A new spherical shallow-water model: building in wave-vortex decomposition, in: Seminar on Recent Developments in Numerical Methods for Atmospheric and Ocean Modelling, 6–10 September, 2004, ECMWF. Available from: <http://www.ecmwf.int/newsevents/meetings/annual_seminar/2004>.

[6] D.G. Dritschel, M.H.P. Ambaum, The diabatic contour advective semi-Lagrangian algorithm, Mon. Weather Rev. (in press).

[7] R. Ford, M.E. McIntyre, W.A. Norton, Balance and the slow quasimanifold: Some explicit results, J. Atmos. Sci. 57 (2000) 1236–1254.

[8] A. Gill, Atmosphere-ocean dynamics, Int. Geophys. Ser. 30 (1982).
[9] B. Haurwitz, The motion of atmospheric disturbances on the spherical earth, J. Mar. Res. 3 (1940) 254–267.
[10] B.J. Hoskins, M.E. McIntyre, A.W. Robertson, On the use and significance of isentropic potential–vorticity maps, Quart. J. Roy. Meteorol. Soc. 111 (1985) 877–946.
[11] M.N. Juckes, M.E. McIntyre, A high-resolution one-layer model of breaking planetary waves in the stratosphere, Nature 328 (1987) 590–596, Corrigendum 58, 949.
[12] M.E. McIntyre, W.A. Norton, Potential vorticity inversion on a hemisphere, J. Atmos. Sci. 57 (1999) 1214–1235, Corrigendum 58, 949.
[13] A.R. Mohebalhojeh, D.G. Dritschel, On the representation of gravity waves in numerical models of the shallow water equations, Quart. J. Roy. Meteorol. Soc. 126 (2000) 669–688.
[14] A.R. Mohebalhojeh, D.G. Dritschel, Hierarchies of balance conditions for the *f*-plane shallow water equations, J. Atmos. Sci. 58 (16) (2001) 2411–2426.
[15] J. Norbury, I. Roulstone (Eds.), Large-scale atmosphere-ocean dynamics, Analytical Methods and Numerical Models, vol. 1, Cambridge University Press, 2002.
[16] L.M. Polvani, J.C. McWilliams, M.A. Spall, R. Ford, The coherent structures of shallow water turbulence: deformation-radius effects, cyclone/anticyclone asymmetry and gravity-wave generation, Chaos 4 (1994) 177–186, 427–430.
[17] H. Ritchie, Application of the semi-Lagrangian method to a spectral model of the shallow water equations, Mon. Weather Rev. 116 (1988) 1587–1598.
[18] A. Robert, The integration of a low order form of the primitive meteorological equations, J. Meteor. Soc. Japan 44 (1966) 237–245.
[19] J. Shipton, D.G. Dritschel, Balance and gravity waves in spherical shallow-water turbulence, J. Atmos. Sci. (under review).
[20] J. Thuburn, Y. Li, Numerical simulations of Rossby–Haurwitz waves, Tellus A 52 (2) (2000) 181–189.
[21] D.L. Williamson, J.B. Drake, J.J. Hack, R. Jakob, P.N. Swarztrauber, A standard test set for numerical approximations to the shallow water equations on the sphere, J. Comput. Phys. (1992) 221–224.